Macromolecules

pubs.acs.org/Macromolecules
Article

Entropic Phase Separation in Polymer–Vitrimer Melts

Alexandros A. Rispo Constantinou,* Bálint Magyari, Giovanni Ianniruberto, Evelyne van Ruymbeke, and Daniel J. Read

Cite This: https://doi.org/10.1021/acs.macromol.6c00893
Read Online

ABSTRACT: Traditional plastics demand a choice between durability (thermosets) and reprocessability (thermoplastics). Vitrimers are a recent class of polymer network combining both of these qualities. Their increased cost of production can be offset by mixing them with a traditional thermoplastic; however, phase separation in such blends can lead to inhomogenous materials. In this paper, we adapt an existing model for the free energy of dissociative polymer networks to their associative, vitrimeric counterpart. We test the accuracy of the model's predictions by comparing them with the results of novel molecular-dynamics simulations. We demonstrate that such melts can undergo phase separation even in the absence of energetic interactions between the components, with a phase diagram qualitatively similar to that of dissociative systems. We furthermore find that—for equal-length chains in the limit of highly functionalized vitrimers—entropic phase separation sets in as soon as two function sites per chain are cross-linked to other chains, such that only loosely cross-linked networks are stable.

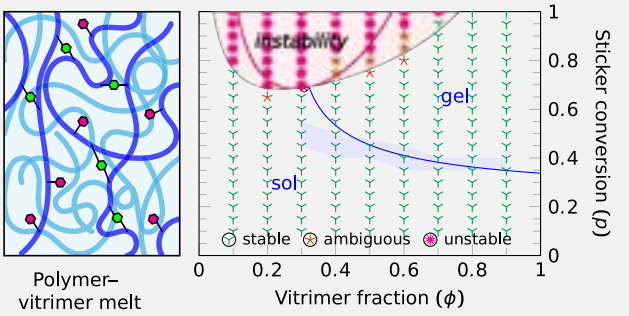

1. INTRODUCTION

Fifteen years ago, Leibler and co-workers[1] first stably synthesized a new class of materials they dubbed 'vitrimers'. These materials have a wide variety of applications,[2,3] which include their use as a recyclable, self-healing alternative to thermosets; as a compatibilizer providing reversible adhesion between immiscible materials; or, mixed with a classical homopolymer, as an additive to improve thermomechanical properties without loss of reprocessability.[4,5] They achieve this remarkable versatility by forming polymer networks much like a thermoset, with a fixed number of cross-links, but capable of reversibly reshuffling cross-link sites to rearrange the network topology. Vitrimers are built from functional copolymers, typically obtained from commercially available monomers with the periodic addition of pendant functional groups (i.e., cross-link–capable sites). A small cross-linking molecule is then added, forming covalent bonds with the functional sites; being highly energetic, these bonds are rarely broken at normal temperatures. However, they can exchange attachment points with other cross-linkers, and do so often, as this reaction has fairly low energy of activation.[6] Sites not occupied by cross-linkers are stoppered by some 'stopper' moiety, which acts as a place-holder to prevent empty sites from reacting haphazardly. The only reaction present in the final material is thus the exchange of attachment points between moieties (cross-linker–cross-linker and cross-linker–stopper). In this way, a dynamic network is formed which rearranges itself topologically yet always maintains a constant overall number of cross-links.

One application of particular interest involves dispersing vitrimers into a classical homopolymer matrix. By carefully selecting the materials involved, the resulting mixture can be made more thermomechanically resistant than a traditional thermoplastic, at a fraction of the cost of a pure vitrimer. Unlike a thermoset with permanent cross-links, this hybrid material is reprocessable and self-healing, thanks to the cross-links' dynamic nature. The anatomy of such a mixture — in the specific case of a polystyrene vitrimer with dioxaborolane moieties — is illustrated in Figure 1. Therein, the cross-linker moiety (C) attaches to functional sites on the vitrimer backbone (B), and the stopper moiety (D) is simply a monofunctional version of the cross-linker, filling up all remaining sites. The fourth component is the matrix (A), which we refer to interchangeably as polymer or homopolymer.

Received: March 27, 2026
Revised: July 21, 2026
Accepted: August 25, 2026

https://doi.org/10.1021/acs.macromol.6c00893
Macromolecules XXXX, XXX, XXX–XXX

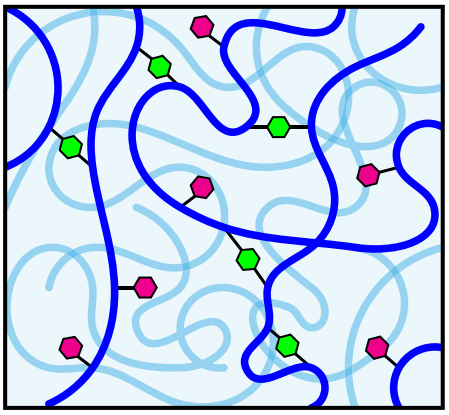

(a) Cartoon of the melt, consisting of the homopolymer (~ / A), the vitrimer backbone (~ / B), the cross-linker moiety (-o- / C) and the stopper moiety (-o / D).

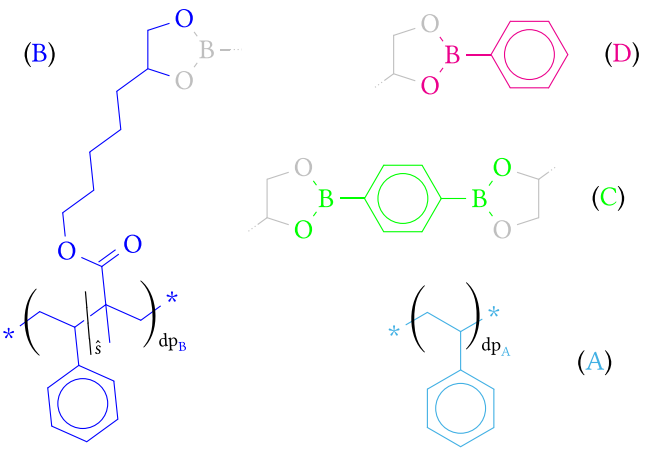

(b) Blend chemistry for a polystyrene-based vitrimer–homopolymer melt with dioxaborolane cross-linker and stopper.

Figure 1. Anatomy of a vitrimer–homopolymer melt.

Studies of such melts are still scarce. However, preliminary evidence suggests that such melts do not mix homogeneously. A study of poly(methyl methacrylate) in an epoxy vitrimer matrix[7] finds clear micron-scale phase separation when the mix is equal parts by weight. Analyses of pure vitrimers[8,9] also detect traces of phase separation at several scales; see de Heer Kloots et al.[10] for a detailed qualitative discussion. Controlling microstructure is important for the practical use of vitrimers: some applications call for well-mixed melts; others rely on specific modes of phase separation.[11] Currently, achieving the correct micro-structure relies on repeatedly iterating experiments and prototypes, a procedure both costly and time-consuming. There is thus a need for a predictive approach to phase separation, which can be achieved through an appropriate theoretical model.

Classical theories of adaptive polymer networks apply to 'dissociative' systems, where the functional sites detach and reattach without the intermediary of cross-linker or stopper moieties. This phenomenon is governed by the energy of association, which is the energy respectively lost or gained by forming or breaking a bond. As such, dissociative networks create or destroy cross-links at will, thereby freely altering their connectivity properties. Since bonds can associate and dissociate, the actual number of bonds (i) will fluctuate around the mean fraction for a material at equilibrium, (ii) may evolve with time when out of equilibrium, and (iii) may not be conserved during processes such as phase separation — in other words, the total number of bonds may change. The mean fraction of bonds associated at any given time is called the 'degree of conversion' (p), and can be predicted at equilibrium by minimizing the free energy of the dissociative system. The result depends on the energy of association as well as on the composition of the mixture; it also varies with temperature, with hotter samples exhibiting fewer bonds (lower p) on average.

In contrast, vitrimers — or 'associative' systems — exist in the limit of high energy of association, when it is almost never favorable to break a bond. This justifies the assumption that, in vitrimers, the total degree of conversion is a conserved quantity: in this approximation, cross-links can change attachment sites, but can never detach spontaneously. A consequence is that vitrimer systems can be treated purely entropically: since the number of bonds remains fixed, the total bonding energy remains constant; hence, it is possible to conceive of an idealized, entropic vitrimer system whose state depends only on the number of microstates generated by the presence of bonds and different chain configurations. Although real vitrimer blends almost certainly also involve energetic effects (e.g. from interaction parameters), it is instructive to investigate first the ideal, entropic case. Therefore, we will restrict the scope of this paper to systems governed entirely by entropic effects, without energetic interactions between any of the four component moieties A–D (cf. Figure 1).

Existing theories mostly describe dissociative networks; nonetheless, similar systems have been extensively studied in the theoretical literature. Approaches include mean-field theory,[12,13] a patchy-particle model,[14] coherent-state field theory,[15] cluster expansions[16] and more; see Tanaka[17] for a review. The mean-field theory due to Semenov and Rubinstein[12] and expanded by Dobrynin[13] is a popular framework. It has been used to study solutions of polyelectrolytes,[18] blends of heteroassociative polymers,[19] mixtures of polymers with compatible functional sites,[20] single-chain nanoparticles with multiple sticker types,[21] and has been to an extent compared with experiments.[22] This approach has the advantage of producing a free-energy function from counting arguments alone, without invoking heavy mathematical artillery. In this paper, we use this framework to arrive at a phase diagram of vitrimer–polymer melts in the absence of enthalpic effects. We will find similar qualitative predictions to those of dissociative systems,[12,13] namely that macro-phase separation occurs whenever the degree of conversion (resp. energy of association) is sufficiently large. In contrast with the dissociative case, however, there are compositions of melt which never undergo separation (generally if the proportion of vitrimer is sufficiently large or small). Furthermore, the separation we predict is fully driven by the entropy of the resulting phases, meaning that it is a purely statistical phenomenon.

Phase separation driven by entropic effects is of course not new. In the polymer literature previous works have considered phase separation induced by differences in chain stiffness, or short-chain branch content in polyolefins. These include lattice-based models,[23,24] field-theoretic approaches[25] and, more recently, simulations.[26,27] However, these studies differ from ours in that the entropic effect is due to changes in the number of local packing configurations available when dissimilar polymers are mixed.

https://doi.org/10.1021/acs.macromol.6c00893
Macromolecules XXXX, XXX, XXX–XXX

Since these effects are local, they can be accounted for via an entropic contribution to the effective χ interaction parameter, as predicted by several of the above models. In contrast, the entropic effect at play in our study concerns changes in the translational entropy and network connectivity as composition is varied. In this sense, the entropic effects in our work are more analogous to those previously identified in polymer–microemulsion networks.[28]

Our work addresses the need for a predictive model of phase separation in vitrimer–polymer melts by providing an initial, simplistic description using the mean-field theory. Thus far, no systematic experimental campaign has been conducted to capture regimes of stability in these melts. To validate our description, we therefore turn to numerical methods. Molecular dynamics simulations have been used extensively to model polymer systems;[29−31] by adding Monte-Carlo–based interactions between selected beads, they have successfully been extended to model dynamic polymer networks.[32−34] While Monte-Carlo simulations have been used extensively to study the *viscoelastic* behavior of vitrimer melts, phase separation remains largely unexplored territory. To our knowledge, this study constitutes the first systematic comparison with simulations of the mean-field–type theory introduced by Semenov and Rubinstein.[12]

The goal of this paper is, therefore, to provide a combined theoretico-simulative approach to predicting macroscopic phase separation in vitrimer–polymer melts, meant to guide experimental exploration of these materials' design space. The paper is structured as follows. In Section 2, we derive a mathematical model for the free energy of a vitrimer–polymer melt devoid of energetic interactions. Section 3 then presents the hybrid Monte-Carlo/molecular-dynamics simulative approach adopted to validate the theory. In Section 4, we compare simulation results with the theoretically predicted incidence of macroscopic phase separation, and discuss possible extensions of the theory. Conclusions are drawn in Section 5.

2. FREE ENERGY MODEL

In this section, we derive the Helmholtz free energy for a vitrimer–polymer melt. For the sake of exposition, and for better comparison with the simulations carried out in Section 3, we will only present a simplified derivation where the small moieties — cross-linker and stopper — are 'phantom' objects which do not occupy any volume. We will discuss how this assumption can be lifted in Section 4.3, with a complete derivation given in the supplementary information (Part A). The resulting, simplified model assumes that the functionalized monomers on every vitrimer chain can directly bond to other functionalized monomers, without the intermediary of a physical cross-linker. We will use the language of previous works on dissociative polymer networks and call these special monomers 'stickers', and define a sticker as 'bonded' if the equivalent functional site is attached to a cross-linker, and 'free' otherwise (Table 1). Though confusing at first, this change in language allows better alignment with existing literature, and makes the link to simulations more straightforward.

Therefore, the melt consists of two species: a homopolymer matrix, chemically inert, and a vitrimeric network of the same chemical nature, every chain of which has s designated stickers. We assume that stickers are uniformly distributed along the chain (i.e., located at equal monomeric intervals), with half an interval at the extremities. To emulate the effect of covalent bonds, we fix the total number of sticker–sticker cross-links ('bonds') to some global value. Since the number of bonds is fixed, and the vitrimer and homopolymer are assumed not to interact energetically, all microstates have the same enthalpy, and the internal energy may be excluded from the computation of the partition function. Even if a system phase separates, with different amounts of cross-linking in each phase, the constant *total* number of bonds (summed over both phases) ensures the total internal energy is constant. As bonds never break without immediately reforming, their association and dissociation can never contribute to the overall energy balance. The calculation thus involves only a conformational or entropic term, counting the number of ways to arrange vitrimer and polymer chains in the melt. The predictions of this simplified model will be shown at the end of Section 2.4, and later compared to the results of simulations in Section 4.1.

Table 1. Conversion between Terminologies

chemical nomenclature	phantom model
functional site	sticker
site with cross-link	bonded sticker
site with stopper	free sticker

2.1. Derivation

We follow in large part the derivation of Semenov and Rubinstein,[12] rewritten in terms of a lattice model. The major difference is that we do not approximate the solvent's effect through its virial coefficients, given that our 'solvent' is actually a polymer matrix. Our basic theory, before the addition of cross-links, is the classical Flory–Huggins theory of polymer melts.

To obtain the partition function, we count the number of ways of arranging the vitrimer and polymer chains on a lattice, subject to the constraint of forming the correct number of sticker–sticker bonds. We start by giving the number of ways of arranging the chains in the absence of such constraints, Ω_{FH}, and later correct it by a combinatorial factor.

Given a lattice of n_0 sites filled with n vitrimer chains, each occupying N sites, and m polymer chains, each occupying M sites, the number of ways of placing these chains on the lattice is given in the mean-field approximation by

$$\Omega_{\mathrm{FH}} := \frac{n_0!}{n_0^{n_0}} \frac{(n_0\zeta_N)^n}{n!} \frac{(n_0\zeta_M)^m}{m!} \tag{1}$$

where the ζ_i represent the number of internal configurations available to the chains on the lattice, uncorrected for excluded volume; hence the explicit dependence on N and M in ζ_N and ζ_M. Equation 1 is a standard result of the Flory–Huggins theory; its derivation can be found in Flory[35] or, for convenience, in the supplementary information (Part A).

If there are c cross-links between stickers (one cross-link for two stickers), the partition function Ω_{FH} needs to be multiplied by the number of ways of forming c distinct sticker pairs, as well as by the probability that the chains are in a configuration allowing that many bonds. Forming c pairs out of $s \times n$ stickers is equivalent to ordering the stickers in a list defined such that the first sticker is paired with the second, the third with the fourth, and so on. The remaining $sn - 2c$ stickers are unpaired. The following diagram illustrates the situation, with each sticker represented by an asterisk (∗).

$$\underbrace{(*,*)\,(*,*)\cdots(*,*)}_{2c \text{ stickers form } c \text{ pairs}} \;\Big|\; \underbrace{*\,*\,*\,*\,*\cdots*}_{sn-2c \text{ stickers remain unpaired}}$$

https://doi.org/10.1021/acs.macromol.6c00893
Macromolecules XXXX, XXX, XXX−XXX

There are $(sn)!$ ways of arranging the stickers in this list, to be corrected by dividing by $c!$ (since the ordering of the pairs doesn't matter), by $(sn - 2c)!$ (since the ordering of the unpaired stickers doesn't matter), and by 2^c (since the ordering of the stickers within a pair doesn't matter).

Next we compute the probability that the chains be in a configuration allowing c bonds. A given bond is allowed if and only if that bond's second sticker occupies one of the x sites on the immediate coordination shell of the first sticker. This happens with probability x/n_0. The event then needs to recur c times, so the probability becomes $(x/n_0)^c$. (The number of cross-link-compatible second sites x depends on the specific geometry of the chains, but is usually taken to be two less than the lattice coordination number, accounting for monomers adjacent to the sticker.)

The full partition function Ω is thus the product of these two factors with Ω_{FH}, namely

$$\Omega = \Omega_{\mathrm{FH}} \times \frac{(sn)!}{2^c\, c!\, (sn-2c)!} \times \left(\frac{x}{n_0}\right)^c \tag{2}$$

To obtain an expression for the entropy, we apply Stirling's formula $z! \sim (z/\mathrm{e})^z$ and take the natural logarithm of Ω. We also wish to rewrite the expression in terms of (independent) intensive variables: one is the volume fraction occupied by vitrimer chains, $\phi := Nn/n_0$; the other is a rescaled version of the volume fraction occupied by bonded stickers: $\psi := 2c/n_0 \times N/s$. We choose the scaling factor N/s on this second quantity so that ψ ranges between zero and ϕ, and the degree of conversion of stickers is $p := 2c/sn = \psi/\phi$. The volume fraction occupied by the polymer is — by conservation of volume — not an independent variable, and indeed is equal to $1 - \phi = Mm/n_0$. Performing these substitutions, and defining $\mathfrak{H}(z) := z\log(z)$ for compactness, the non-dimensional free energy per lattice site $f := -\log(\Omega)/n_0$ is given by

$$\frac{N}{s} f \approx \frac{1}{s}\left[\mathfrak{H}(\phi) + \frac{N}{M}\mathfrak{H}(1-\phi)\right] + \mathfrak{H}(\phi-\psi) + \frac{1}{2}\mathfrak{H}(\psi) - \mathfrak{H}(\phi) \tag{3}$$

Here and elsewhere in the text we have freely removed from the free energy both constants and terms linear in the concentration variables (ϕ, ψ), as they have no effect on the resulting predictions (cf. Section 2.4). It is worth emphasizing that the expression Nf/s in eq 3 is independent of any lattice parameters. Note also that the behavior of the system does not directly depend on the lengths of the component chains, but only on their ratio M/N.

Heuristically, this expression for the free energy can be seen as the interplay between two competing influences: the first term in parentheses — scaling as $1/s$ — is convex, encouraging stable behavior, whereas the rest of the expression pushes for instability. As s increases, the unstable influence becomes more prominent and the region of instability grows, leaving only a small island of stability near $(\phi, \psi) = (1, 0)$.

A variant derivation, due to Dobrynin,[13] suggests that the expression in eq 3 takes into account the presence of cycles in the network; the details of this, along with the full derivation for volume-occupying cross-linker and stopper, are given in the supplementary information (Part A).

2.2. Nearest-Neighbor Correction

The partition function provided in eq 2 assumes that the second sticker within each pair has equal probability of lying anywhere in the system volume. Whilst good for stickers disconnected from each other (or only connected through a long enough path), this assumption is deficient when stickers are separated by short lengths of vitrimer backbone. In this case, the stiffness of the chains affects sticker distributions. The effect is particularly salient when the vitrimer is dilute in the matrix, and stickers mostly see stickers from the same chain in their immediate vicinity. Following both Semenov and Rubinstein[12] and Dobrynin,[13] we model these local bonds through their leading-order behavior, when stickers pair with their nearest neighbor along the chain (Figure 2). Longer-range bonds are polynomially suppressed by the entropic cost of forming a loop in the polymer, with scaling $(\text{loop length})^{-3/2}$.

First we calculate the contribution to the partition function due to nearest-neighbor bonds. Let a fraction q of the s stickers on a given vitrimer chain be involved in nearest-neighbor pairs. To calculate how many ways this can happen, imagine having a list of the $(s - qs)$ free stickers and $qs/2$ cross-linked sticker pairs on that chain, and asking the number of ways to rearrange these. By a 'stars-and-bars' argument,[36] this is the same as taking $(s - qs) + qs/2$ objects, and selecting $qs/2$ to be pairs. The number of ways of doing this is simply the binomial coefficient $(s - qs/2)!/[(qs/2)!\ (s - qs)!]$. However, forming $qs/2$ nearest-neighbor pairs comes with an entropic cost, as the configurations that the two bonded stickers can have relative to each other are reduced. This cost can be accounted for by multiplying the partition function by the probability $\mathbb{P}[l_{N/s}]$ of forming a loop of length $l_{N/s}$, repeating as many times as there are loops $(qs/2)$. The product of these two expressions is the amount by which each vitrimer chain modifies the partition function due to local bonds between nearest-neighbor stickers. For the full partition function, we multiply eq 2 by n copies — one for each vitrimer chain — of this local-bond correction term. The result is

$$\Omega = \Omega_{\mathrm{FH}} \times \left(\frac{(s-qs/2)!}{(qs/2)!\ (s-qs)!}\, \mathbb{P}\left[l_{N/s}\right]^{\frac{qs}{2}}\right)^n \times \left(\frac{x}{n_0}\right)^{\tilde{c}} \frac{(\tilde{sn})!}{2^{\tilde{c}}\tilde{c}!\ (\tilde{sn}-2\tilde{c})!} \tag{4}$$

where $\tilde{sn} = sn - qsn$ and $\tilde{c} = c - qsn/2$ are the values reduced by the number of stickers (resp. cross-links) involved in local,

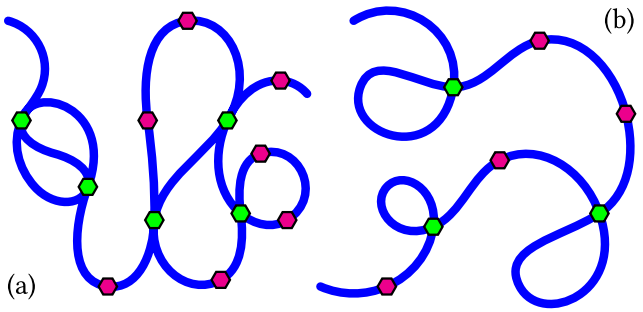

Figure 2. Generic same-chain linking (a) vs nearest-neighbor only (b).

https://doi.org/10.1021/acs.macromol.6c00893
Macromolecules XXXX, XXX, XXX–XXX

nearest-neighbor pairs. As before, eq 4 can be used to provide the free energy, yielding

$$\frac{N}{s}f = \frac{1}{s}\left[\mathfrak{H}(\phi) + \frac{N}{M}\mathfrak{H}(1-\phi)\right] + \mathfrak{H}(\phi-\psi) + \frac{1}{2}\mathfrak{H}(\psi - q\phi) - \mathfrak{H}\left(\left[1-\frac{1}{2}q\right]\phi\right) + \frac{1}{2}\mathfrak{H}(q\phi) + \frac{1}{2}q\phi\log\left(\frac{2}{ke}\right) \tag{5}$$

The first line is identical to its equivalent in eq 3, the second line has an equivalent but now depends on q, and the third line is entirely new. We recover eq 3 in the limit $q \to 0$, namely when all cross-links are to other vitrimer chains. (We have assumed so far that the cross-linker is two-sided: a similar expression to eq 5 holds when the cross-linker is of arbitrary functionality; this derivation is given in the supplementary information, Part C.)

In eq 5, the fraction q of local cross-links is an unconstrained variable obeying only the inequality $q \le p$. We therefore fix its value by extremising the free energy over q, namely by setting $\partial f/\partial q = 0$. The resulting optimality condition

$$\frac{(2-q)q}{p-q} = \frac{k}{\phi} \tag{6}$$

is controlled by a parameter $k := \mathbb{P}\left[l_{N/s}\right] \times 4N/(sx)$ measuring the propensity for local bonding. Equation 6 can be solved to give

$$q = \frac{k+2\phi}{2\phi}\left(1-\sqrt{1-\frac{4kp\phi}{(k+2\phi)^2}}\right) \tag{7}$$

A good approximation is afforded by linearizing q with respect to p, yielding $q \approx kp/(k+2\phi)$. This approximation is excellent so long as $4kp\phi/(k+2\phi)^2 \ll 1$; it is at its worst when $\phi = k/2$ and $p = 1$, with maximal error $3/2-\sqrt{2}$, or about 9%. This error reduces quickly with decreasing p, being just over 5% by $p = 0.8$, and has little impact on the majority of the explored phase space; for typical values of p in practical applications, on the order of a few units per cent, the error is less than one in five thousand. This approximation greatly increased the speed in our numerical computation by facilitating evaluation of the free energy and its derivatives.

We see from the linearization that the simpler expression in eq 3 is most accurate when $k \to 0$, which occurs in the limit of greater inter-sticker spacing since $k \sim (N/s)^{-1/2}$ (see next section). Note also that as the solution becomes more dilute, we see q approach p: in other words, local bonds dominate the cross-linking behavior, and percolation becomes increasingly difficult.

2.3. Local Bonding Propensity

The parameter k controlling the local bonding propensity remains a free parameter of this theory. Some intuition for it can be afforded by rephrasing it in terms of material properties of the vitrimer. In this section, we provide an interpretation through a simplified scaling argument then, for reference, perform the calculation exactly for ideal (Gaussian) vitrimer chains. The latter, exact result is not essential to the discussion.

Consider a segment of chain between two stickers, consisting of $l_{N/s}$ Kuhn segments, each of length b. To find $k := \mathbb{P}\left[l_{N/s}\right] \times 4N/(sx)$, we need the probability $\mathbb{P}\left[l_{N/s}\right]$ of the segment's two ends lying within a bond volume (v_b) of one another. This probability is proportional to the bond volume v_b when v_b is small, since the underlying segment-end distribution is approximately constant over small regions. The maximum value that the bond volume can take — at which the probability should be unity — scales as the cube of the chain segment's root-mean-square end-to-end radius $R_s \sim b\sqrt{l_{N/s}}$, which characterizes the typical distance by which segment ends are likely to be separated. Thence the scaling $\mathbb{P}\left[l_{N/s}\right] \sim v_b/R_s^3$. Replacing the bond volume with its lattice-based equivalent $v_b = xv_0$, we obtain the scaling law $k \sim v_s/R_s^3$, where $v_s = v_0N/s$ is the volume taken up by the inter-sticker chain segment, or equivalently the volume of vitrimer chain per sticker. Interpreting R_s^3 as the volume spanned by the chain section between two stickers, we find that $1/k \sim R_s^3/v_s$ is (roughly) the typical number of stickers within a volume R_s^3 for a pure vitrimer system — i.e., in the absence of a homopolymer matrix. Its square $1/k^2$ is also known as the 'invariant degree of polymerization'[37] for that inter-sticker segment.

The packing length P of a polymer chain corresponds to the length scale on which a chain fully fills its pervaded volume, and is defined as the ratio of the chain's displaced volume to its root-mean-square end-to-end radius.[38] Using the chain segment between adjacent stickers, we have $P \sim v_s/R_s^2$. The consequent scaling

$$k \sim P/R_s \tag{8}$$

gives a further intuitive interpretation of k as the reciprocal inter-sticker distance, measured in units of the packing length. This can be understood as encoding the fact that stickers within the same packing blob are easy to cross-link without losing much entropy; the more blobs they are separated by, however, the more costly (and therefore rare) cross-links become, and $k \to 0$.

For reference, we now compute k theoretically for an ideal chain.[39,40] Recall that the Green's function $\mathcal{G}_l(\mathbf{r})$ for an isolated phantom chain of l effective bonds of length b is given by the expression

$$\mathcal{G}_l(\mathbf{r}) = \left(\frac{2\pi}{3}lb^2\right)^{-3/2}\exp\left(-\frac{3\|\mathbf{r}\|^2}{2lb^2}\right) \tag{9}$$

where $\mathbf{r}$ is the end-to-end vector of the chain. Requiring that the chain ends lie within a volume v_b of one another is then equivalent to integrating over the locality operator $v_b\,\delta$, where δ is the Dirac delta. Thus

$$\mathbb{P}[l] = \int_{\mathbb{R}^3} \mathrm{d}^3\mathbf{r}\; v_b\,\delta(\mathbf{r})\,\mathcal{G}_l(\mathbf{r}) = \frac{v_b}{b^3}\left(\frac{2\pi}{3}l\right)^{-3/2} \tag{10}$$

The last step is then to express the inter-sticker distance in units of the effective bond length b. This is simply the number of Kuhn segments between successive stickers, obtained by dividing the volume $v_s = v_0N/s$ of an inter-sticker chain segment by the volume v_K of a Kuhn segment, giving $l_{N/s} = N/s \times v_0/v_K$.

https://doi.org/10.1021/acs.macromol.6c00893
Macromolecules XXXX, XXX, XXX–XXX

Substituting all of these into $k := \mathbb{P}\left[l_{N/s}\right] \times 4N/(sx)$ and again replacing $\nu_b = x\nu_0$ gives

$$k = \frac{3\sqrt{6}}{\pi^{3/2}} \sqrt{\frac{s}{N}} \left(\frac{\nu_K}{\sqrt[3]{\nu_0}\, b^2} \right)^{3/2} \tag{11}$$

with numerical prefactor about 1.34. In particular, note the scaling $k \sim \sqrt{s/N}$, implicit in eq 8.

2.4. Phase Diagram

From the free energy, we can obtain the phase diagram, displaying the system's behavior for the entire phase space $(\phi, p) \in [0, 1]^2$, with $p = \psi/\phi$. We first describe how the various features of the diagram are computed, before presenting a typical phase diagram at the end of the section.

2.4.1. Methodology. The spinodal curve is the transition from local stability to local instability, and occurs when the free energy goes from concave in both directions to convex in at least one; we find this curve by numerically searching for the zero contour of the Hessian determinant of the free energy $f = f(\phi, \psi)$. Namely, we solve

$$f_{,\phi\phi} f_{,\psi\psi} - \left(f_{,\phi\psi}\right)^2 = 0 \tag{12}$$

where the subscript comma denotes differentiation with respect to subsequent variables. The binodal, marking the transition from true stability (global convexity) to a metastable state (locally convex but globally concave) is less straightforward, but is guaranteed to intersect the spinodal in at least one point, called the 'plait point'. The plait point is a particular type of critical point in liquid–liquid systems corresponding to the location where binodal points — the extremities of tie-lines, i.e., coexisting phases — become identical and coalesce.[41,42] Our methodology begins by obtaining this intersection by simultaneously solving the aforesaid spinodal condition — eq 12 — alongside an equation specific to the plait point:

$$f_{,\psi\psi\psi} f_{,\phi\psi} f_{,\phi\phi} - 3\left(f_{,\phi\psi}\right)^2 f_{,\phi\psi\psi} + 3 f_{,\phi\psi} f_{,\psi\psi} f_{,\phi\phi\psi} - \left(f_{,\psi\psi}\right)^2 f_{,\phi\phi\phi} = 0 \tag{13}$$

Equation 13 corresponds to the statement that the plait point is an inflection point on the spinodal curve; it can be derived from the condition $(\mathbf{t} \cdot \nabla)^3 f = 0$, where $\mathbf{t} \propto [-f_{,\phi\psi}\, f_{,\phi\phi}]^\top$ is any tangent to the spinodal and $\nabla := [\partial_\phi\ \partial_\psi]^\top$ is the gradient on the phase space of conserved variables. Then, the binodal is found by imposing (and numerically solving for) equality of the chemical potentials $\mu_\phi := f_{,\phi}$, $\mu_\psi := f_{,\psi}$ and osmotic pressure $\Pi := \phi\mu_\phi + \psi\mu_\psi - f$ across both phases, according to the common-tangent construction. Straight-line segments joining such solutions are known as tie-lines, and conservation of the phase parameters (ϕ, ψ) implies that any unstable state lies on the tie-line into whose extremities it will separate. Therefore, we use a stepping algorithm to generate the tie-lines by guessing an unstable state and finding the tie-line passing through it, starting at the plait point and always moving perpendicularly to the last tie-line found. The set of tie-line extremities forms the binodal. (This is one of several possible approaches: Archer et al.[43] outline a similar algorithm, based on sweeping through chemical potentials instead of unstable states; other options are the iterative method, as in Qian et al.,[44] or the method of dominance analysis.[45]) Our algorithm is prone to pitfalls such as local optima and three-phase separation; to avoid these, we used a more robust but less accurate method to first visualize the region of instability. Namely, we computed the lower convex envelope of the free energy surface, since it is flat in i directions when coexistence is between $(i + 1)$ phases, $i \in \{1, 2\}$. We are grateful to Peiwen Ren[46] for his advice and example code performing this computation. Finally, the mean-field percolation transition is obtained by solving an appropriate Flory–Stockmayer condition[13,47]

$$p - q = \frac{1}{(1-q)s - 1} \tag{14}$$

for the sticker conversion p as a function of the vitrimer fraction ϕ, with $q = q(p, \phi)$ from eq 6. Under this condition, we say a system is in a 'sol' state when vitrimer chains form finite clusters, and in a 'gel' (or percolated) state as soon as there is one (infinite) cluster spanning the whole system. Equation 14 is derived by assuming clusters are tree-like, with no cycles, and computing the expected number of new chains at each generation: the criterion for percolation is when this value is greater than unity.[48]

2.4.2. Phase Diagram. Figure 3 shows the resulting phase diagram for parameter values chosen to match the simulations performed in Section 3. The diagram displays both a percolation (sol–gel) transition and a miscibility dome. Any system with volume fraction and sticker conversion lying outside the miscibility dome will be single phase: either a sol below the gelation transition or a gel above it. Within the miscibility dome, the system will phase separate. We note that instability tends to set in as cross-links are added to the system, globally raising p. In the upper part of the phase diagram, within the miscibility dome, the two phases resulting from phase separation are indicated by the extremities of the tie-lines that intersect the system-averaged volume fraction, ϕ, and sticker conversion, p. On increasing p away from the plait point, these tie-lines increasingly share the same local p value after splitting. For this

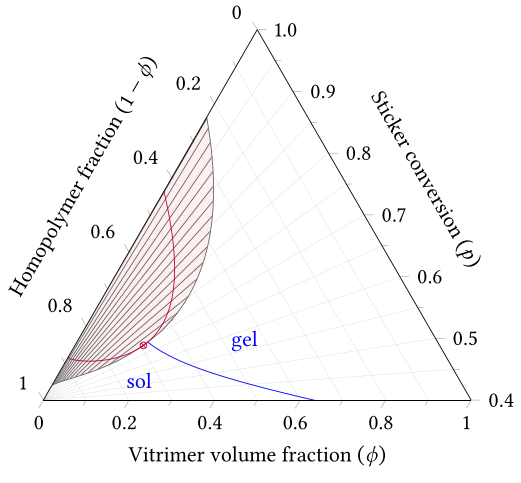

Figure 3. Phase diagram obtained from eq 5 with $M = N = 20$, $s = 5$ and $k = 0.48$, showing the gelation transition (blue), spinodal curve (red), binodal curve (gray), tie-lines (gray segments) and plait point (symbol ⊗). Data are plotted on 'pinched axes' as the phase space is naturally triangular. On these axes, lines of constant p are rays emanating from the left-hand corner, whereas lines of constant ϕ connect a value on the vitrimer axis with its complement on the homopolymer axis. Note that we show only a subspace $p \geq 0.4$.

https://doi.org/10.1021/acs.macromol.6c00893
Macromolecules XXXX, XXX, XXX–XXX

choice of parameters, most trial phases separate into both sol and gel phases, since the percolation transition passes very near to the plait point. The separation into sol and gel appears to be a common feature of these polymer–vitrimer systems, as will later be discussed for $s \gg 1$ (Section 4.4). However, the gelation line does not exactly meet the plait point, and for these parameters we predict a minority of systems close to the plait point that phase separate into two sol phases.

Qualitatively, our phase diagram is similar to those of Semenov and Rubinstein[12] and Dobrynin.[13] Heuristically, the globally conserved sticker conversion (p) in associative networks can be compared to the attractive volume of a bond (λ, which depends exponentially on the energy of association) in dissociative networks: both control the density of the resulting network, and for the purposes of visualization can be plotted as the ordinate of the phase diagram against the vitrimer concentration variable on the abscissa. Doing so, we observe the same topological features, namely two-phase regions for high p (resp. λ) often — but not always — separating between a sol and a gel phase. Of course, the difference in control parameters between associative and dissociative polymer networks means that the correspondence is imperfect, and predictions can only ever be compared qualitatively.

3. SIMULATION METHODOLOGY

To validate the theoretical framework proposed in Section 2, molecular dynamics simulations were performed to investigate phase separation phenomena in purely entropic vitrimer–homopolymer blends. Here, we present simulations of the simplified model without the inclusion of explicit cross-linker molecules. We employ the widely adopted coarse-grained Kremer–Grest bead-spring model[29] utilizing fully flexible chains without angular potentials. A system of 2000 chains, each of length $N = 20$ beads, were initialized in a cubic periodic box with size $L \gg 5\ R_g$ (where R_g is the mean radius of gyration), such that the monomer number density was $\rho = 0.85\ \sigma^{-3}$.

The vitrimer volume fraction ϕ was varied in the interval $\phi \in [0.1, 0.9]$, in steps of 0.1. Vitrimer chains are distinguished from homopolymers by the inclusion of evenly distributed monofunctional associative groups (stickers) along the backbone. The only difference between stickers and regular beads is the stickers' ability to form crosslinks with a maximum of one other sticker. Regarding their mass and physical interactions, the two types of monomer are identical. Each vitrimer chain contains five stickers, which are distributed along the twenty-bead backbone at positions 2, 6, 10, 14, and 18. A functionalization of five stickers per chain ensures the system resides well above the percolation threshold (given sufficiently large sticker conversion is achieved), thereby minimizing possible topological defects. Furthermore, it allows reasonable computation times.

3.1. Equilibrium Molecular Dynamics

Excluded volume interactions between non-bonded beads are modeled by the purely repulsive Weeks–Chandler–Andersen (WCA) potential,[49] a Lennard-Jones (LJ) potential truncated and shifted at $r_c = 2^{1/6}\ \sigma$:

$$U_{LJ}(r) = \begin{cases} 4\epsilon\left[\left(\frac{\sigma}{r}\right)^{12} - \left(\frac{\sigma}{r}\right)^{6}\right] + \epsilon & \text{for } r \le r_c \\ 0 & \text{for } r > r_c \end{cases} \quad (15)$$

where r denotes the inter-particle distance, while ϵ and σ represent the fundamental energy and length scales respectively. The simulations employ standard reduced units with bead mass m_0 and Boltzmann constant k_B. Consequently, time is expressed in units of $\tau := \sigma\ (m_0/\epsilon)^{1/2}$.

Connectivity between adjacent backbone monomers, as well as the reversible cross-links formed between stickers, is governed by a finitely extensible non-linear elastic (FENE) potential.[29] This potential superposes the attractive entropic spring with the purely repulsive WCA component to prevent 'bond crossing' (i.e., bonds passing through each other), thus respecting topological constraints:

$$U_{FENE}(r) = \begin{cases} -\frac{1}{2}KR_0^2 \log\left[1-\left(\frac{r}{R_0}\right)^2\right] + U_{LJ}(r) & \text{for } r < R_0 \\ \infty & \text{for } r \ge R_0 \end{cases} \quad (16)$$

where $K = 30\ \epsilon/\sigma^2$ is the spring constant and $R_0 = 1.5\ \sigma$ represents the maximum bond length.

The above interaction potentials mean that the simulations are not purely entropic, and include some energetic (enthalpic) contributions. However, we omit any excess energies of mixing between the homopolymer and vitrimer species (i.e. $\chi = 0$) by employing the same non-bonding interactions between beads of the two species and by using the same bonding potential for both species. The 'phantom' nature of the cross-links ensures that there is also no excess energy of mixing between the cross-links and anything else. Hence, entropy is the dominant factor driving any phase separation observed.

Prior to the activation of reversible cross-linking, the polymer melt underwent a multi-stage equilibration protocol maintained at a reduced temperature $T^* = 1\ \epsilon/k_B$ using a Langevin thermostat ($\tau_{damp} = 0.1\ \tau$). To eliminate initial steric overlaps and thermally equilibrate the system, non-bonded interactions were initially governed by a soft repulsive potential. This relaxation phase proceeded for a total of 2×10^8 time steps, beginning with an integration step of $\delta t = 0.001\ \tau$ which was subsequently increased to $\delta t = 0.005\ \tau$ to accelerate relaxation. Following the removal of high-energy overlaps, the standard Lennard-Jones potential of eq 15 was restored, and the system was equilibrated for a further 10^8 time steps with $\delta t = 0.001\ \tau$.

To closely control sticker conversion, we developed a controlled cross-linking procedure. Every 10 time steps, unreacted stickers were allowed to form a maximum of 1 bond with another sticker using the fix bond/create command available in LAMMPS.[50] The capture radius was set to $R_{min} = 1.4\ \sigma$ to restrict bonding to the first coordination shell, and prevent high energy bonds from forming near R_0. Secondly, the probability of creating a bond between two candidate stickers was set to $P_{bond} = 0.0001$ to allow the gradual build-up of cross-linking density. Sticker conversion (p) was monitored using an external Python script; as soon as the desired cross-linking density was achieved, bond creation was turned off and the mixture was equilibrated in a canonical (NVT) ensemble with time step $\delta t = 0.01\ \tau$ for a total of 10^8 time steps. The bond potential of the formed cross-links is described by eq 16. At this stage, all cross-links between stickers were permanent in nature.

Following equilibration and cross-linking, dynamic bond exchange reactions were activated. These measurement runs were conducted in a canonical ensemble, where temperature

https://doi.org/10.1021/acs.macromol.6c00893
Macromolecules XXXX, XXX, XXX–XXX

was maintained at $T^* = 1\ \epsilon/k_B$ using a Langevin thermostat ($\tau_{damp} = 0.5\ \tau$). Newton's equations of motion were integrated with a time step of $\delta t = 0.01\ \tau$ for a total duration of 10^8 time steps. Every 10^3 time steps, bond exchange reactions were allowed to occur using the algorithm described in Section 3.2. Initiating data collection immediately upon the activation of bond exchanges allowed us to monitor the phase separation kinetics in real time, capturing the system's evolution from the precise moment topological reconfigurations began.

3.2. Bond Exchange Reactions

Vitrimers are classified as associative covalently adaptive networks (asso-CANs).[3] A defining characteristic of this class of material is the strict conservation of cross-link number, maintained through an exchange mechanism where bond cleavage is immediately followed by bond formation.[9] To capture this topology-altering behavior in the melt state, hybrid Monte-Carlo/molecular dynamics (MC/MD) algorithms have been used extensively.[32−34,51,52] Building upon the framework established by Cui et al.,[32] we extended their MC/MD algorithm to explicitly incorporate exchange reactions involving non-bonded, 'free' stickers.

Bond exchange can occur through two distinct reaction pathways. A 'bond swap' (Figure 4a) involves the metathesis between two existing cross-linked sticker pairs, whereas a 'bond shift' (Figure 4b) is facilitated by the presence of a free sticker in the immediate vicinity of a bonded pair. Crucially, both reaction types are subject to a strict proximity criterion, requiring all participating stickers to be within a defined cut-off radius $r_c = 1.12\ \sigma$. This cut-off value corresponds to the minimum of the WCA potential ($2^{1/6}\ \sigma$), representing the direct contact distance between non-bonded stickers. This strict spatial constraint for bond exchange attempts serves two purposes: first, it mimics the steric requirements of an associative reaction mechanism, ensuring the new bonding partner is in the immediate coordination shell; second, it ensures that newly formed cross-links are created near their equilibrium length ($\approx 0.96\ \sigma$), minimizing high-energy stretched states and eliminating the possibility of bond crossing upon formation of new cross-links. Consequently, the local spatial distribution of stickers dictates the eligibility of specific sites for exchange events.

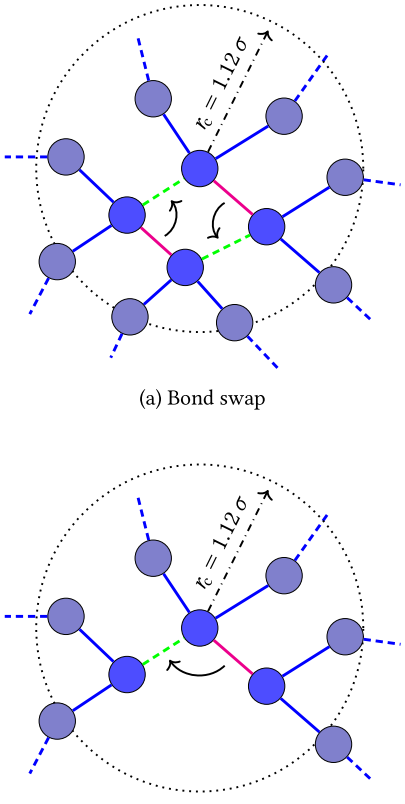

(a) Bond swap

(b) Bond shift

Figure 4. Bond exchange reactions (BER).

For each possible proposed move, the change in potential energy is calculated as:

$$\Delta U = \sum U_{FENE}^{new}(r) - \sum U_{FENE}^{old}(r) \tag{17}$$

where $\sum U_{FENE}^{new}(r)$ and $\sum U_{FENE}^{old}(r)$ are the cumulative FENE potentials of the newly proposed (post-exchange) and the original (pre-exchange) bonds, respectively. For both reaction pathways depicted in Figure 4, two distinct new configurations are possible. Candidates were screened by energy minimization: namely, we retained only the configuration with the lowest ΔU.

The acceptance of the proposed bond exchange reaction (BER) is then governed by the standard Metropolis criterion.[53] Moves resulting in a net reduction of potential energy ($\Delta U \leq 0$) are accepted unconditionally, whereas energetically unfavorable ($\Delta U > 0$) BERs are only accepted with an exchange probability

$$P_{acc} = \exp\left(-\frac{\Delta U}{k_B T^*}\right) \tag{18}$$

To eliminate the possibility of bond exchange reversals within a given integration cycle, stickers that have participated in a successful exchange are excluded from further bond exchange attempts during that cycle. This means that each sticker is limited to a maximum of one bond topological change per MC step.

Strict detailed balance is violated in the algorithm due to the sequential processing of bond exchange candidates, as the exclusion of reacted stickers from subsequent moves within the same time step introduces a non-Markovian dependency on the random iteration order. Nonetheless, the bond exchange reaction algorithm does satisfy the weaker criterion of global balance, which is the necessary and sufficient requirement for Monte-Carlo simulations.[54] On the other hand, when screening the two proposed configurations by energy minimization, a deterministic choice is introduced which technically violates the balances.

Since the difference in potential energy between the two candidates is generally a multiplicative factor, the higher energy candidate would have an acceptance probability several orders of magnitude smaller due to the exponential suppression in eq 18. Therefore, the error introduced by this choice is negligible, and it has the benefit of allowing a significant speed-up in the Monte Carlo algorithm. Thus, this preference towards lower energy transitions identifies dominant reaction pathways, effectively filtering out statistically negligible high-energy transitions. This is applicable for the temperatures generally used in Kremer–Grest simulations ($T^* \lesssim 2\ \epsilon/k_B$).

https://doi.org/10.1021/acs.macromol.6c00893
Macromolecules XXXX, XXX, XXX−XXX

3.3. Inferring Stability

In simulations, it is possible to observe the development of phase separation over time. Starting from an equilibrated, permanently cross-linked network, BERs are turned on and the measurement run starts. The state of the system is inferred at regular time intervals by recording atom coordinates and measuring the distribution and local concentration of beads belonging to vitrimeric chains (both ordinary beads and stickers).

Local properties are calculated by discretizing the simulation box into $7^3 = 343$ equal-volume subdomains. To mitigate bias arising from arbitrary boundary placement, the discretization grid was shifted incrementally along all three axes in steps of one-tenth the subdomain side length. These choices — dividing each side of the simulation box into seven equally sized segments and performing ten grid shifts in each dimension — were guided by two considerations. First, both numbers are coprime, ensuring that no two sampled configurations are identical. Second, splitting the simulation box into seven equal segments along each axis yields a subdomain length of approximately 5 σ, which is large enough to contain a sufficient number of beads to average over, while remaining small enough to produce observable differences between subdomains. Taking into consideration the periodic boundary conditions, this generates an ensemble of 343 000 subdomains. Here, we describe three distinct methods of determining stability from these discretized subdomains.

3.3.1. Distribution Plots. The simplest way to infer the stability of a system is by looking at the number distributions of vitrimeric beads in the (equally sized) subdomains. Stable systems exhibit the expected Gaussian-like distribution, whereas for unstable systems, a split in the distribution is observed, indicative of two distinct phases forming within the melt.

The development of these distributions over time (Figure 5) can give information regarding the rate at which phase separation is developed and when equilibrium is reached. Results reveal that equilibration is invariably reached by the half-way point of the entire simulation (10^8 time steps), with only slight, stochastic deviations observed afterwards.

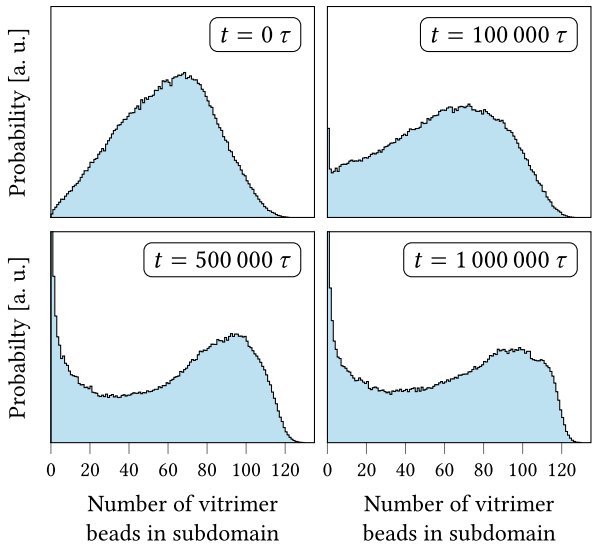

Figure 5. Atom count distribution of vitrimeric beads at four different times during simulation ($\phi = 0.5$, $p = 0.95$). The entire simulation lasted a total of $t = 10^6$ τ, or 10^8 time steps.

Distribution plots prove useful to determine phase separation for well separated systems, where both phases occupy reasonable fractions of the simulation box. For such systems, the distribution plots show clear bimodal distributions. However, for 'edge' cases where bimodality is not apparent, more advanced tools are needed to quantitatively determine phase separation. For this purpose, two alternative methods to infer stability are presented, based on the spatial correlation function and on density variance, respectively.

3.3.2. Spatial Correlation. The stability of the systems were primarily determined from the spatial correlation function. First, we calculate the local composition $\phi(i)$ of the i^{th} subdomain, defined as the proportion of beads in the subdomain that belong to vitrimer chains. This is then correlated with that of all other subdomains as a function of their center-to-center Euclidean distance r according to the formula $\sum_{ij}[\phi(i) - \phi][\phi(j) - \phi]$, where ϕ is the global average composition and the sum is taken over all subdomain pairs (i, j) separated by a fixed distance r. An example of this correlation is shown in Figure 6 for $\phi = 0.5$.

Formally, for a macroscopic system, phase separation would correspond to an infinite correlation length appearing in the system. Non-phase-separated systems would then have a spatial correlation function that decays to zero over a finite distance. Unfortunately our simulations are necessarily finite, with a simulation box made even smaller by its periodic boundaries. This means that: (i) the largest correlation length available corresponds to about half the diagonal of the simulation box, i.e. about 30 σ; (ii) a phase-separated system will have strong positive correlations in composition up to around half the simulation box size, and negative correlations at large distances because of the overall mass conservation in the finite box; but (iii) such negative correlations are also observed as we approach the region of instability in parameter space, because the diverging correlation length quickly approaches the simulation box size. As a result, it is difficult to distinguish the exact point at which phase separation occurs in a finite simulation box: for intermediate cases it may be impossible to decide between a system with long correlations near the phase-separated state, and a system that is actually phase separated. Hence, plotting the spatial distribution function for different values of p gives a continuum of curves rather than a discontinuous change at phase separation. As a practical choice, we decided to take an anticorrelation of –0.1 at large distances as a heuristic criterion

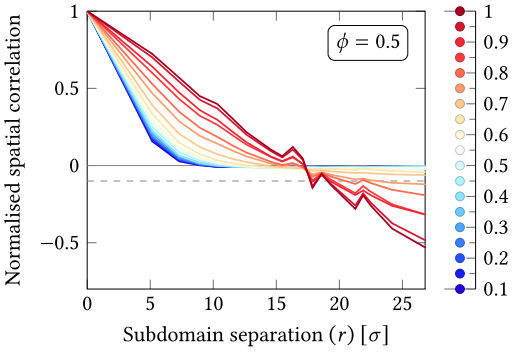

Figure 6. Spatial correlation, for $\phi = 0.5$ and different sticker conversions p, as a function of the distance between subdomain centers. The cut-off point for determining stability is indicated by the horizontal dashed line. The same plots for other values of ϕ can be found in the supplementary information (Part D).

https://doi.org/10.1021/acs.macromol.6c00893
Macromolecules XXXX, XXX, XXX–XXX

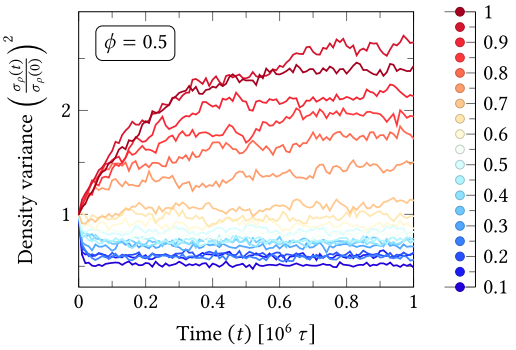

Figure 7. Density variance as a function of time for $\phi = 0.5$ at different sticker conversions p. The same plots for other values of ϕ can be found in the supplementary information (Part D).

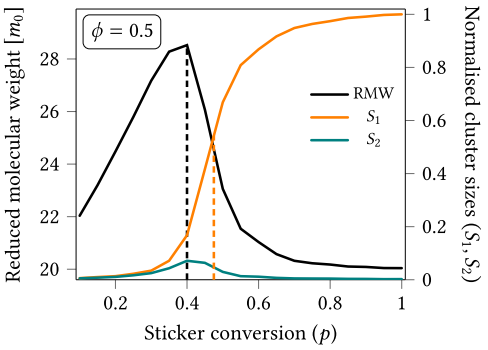

Figure 8. Percolation transition measurements for $\phi = 0.5$. Black curve: reduced molecular weight (RMW); orange curve: normalized largest cluster size (S_1); teal curve: normalized second largest cluster size (S_2). Dashed lines indicate the maximum of the RMW and the inflection point of S_1. The same plots for other values of ϕ can be found in the supplementary information (Part D).

for phase separation. It should be noted that this value is most likely size-dependent and may require adjustment for different box volumes. As can be seen from Figure 6, this criterion also corresponds roughly to the point where the zero of the spatial correlation function approaches that found for the clearly phase separated systems (at larger p).

3.3.3. Density Variance. To support the conclusions drawn from the spatial correlation on the stability of a system, we also look at the change in density variance over time. It is defined as $\sigma_\rho(t)^2 = \langle \rho_i(t)^2 \rangle - \langle \rho_i(t) \rangle^2$, where $\rho_i(t)$ is the vitrimer bead density for each subdomain i at time t, and $\langle \cdot \rangle$ is the average over subdomains; this definition implies $\sigma_\rho(t)^2 \propto \sum_i [\phi_i(t) - \phi]^2$, where ϕ is the global average composition and the sum is over subdomains i. When normalized by the density variance at $t = 0$ (the moment before which only permanent cross-links existed between stickers), stable and unstable configurations show opposing behavior.

Figure 7 shows the density variance as a function of time for systems with $\phi = 0.5$. The different lines correspond to different sticker conversions (p). Systems that phase separate show an increase in their normalized density variance over time, until a stable plateau is reached halfway through the simulation. An increase in density variance is indicative of melt heterogeneity (phase separation). Conversely, stable blends show a decrease in variance, synonymous with increased homogeneity and therefore stability. We classify systems into three categories according to the value of their density variance at large times: less than 1, stable; between 1 and 1.5, ambiguous; above 1.5, unstable. We note, as we did for spatial correlation, that these thresholds may change depending on the volume of the simulation box.

When looking at Figure 7 a question arises: why does the density variance for stable systems decrease relative to the starting state? This phenomenon can be attributed to the increased mobility induced by BERs. By turning on BERs, the system is able to equilibrate further than it was previously capable to with permanent cross-links, and the increased mobility of beads permits a more homogeneous state. This argument supports the idea that an increase in density variance can be attributed to phase separation.

3.4. Percolation Transition

It is also important to conceptually validate the Flory–Stockmayer prediction of the gelation line. Gelation is defined as the first point at which an infinitely large network forms, spanning the entirety of the sample. In MD simulations, this is the moment at which the probability of finding a cluster spanning the entire simulation box becomes non-zero by forming an 'infinite' network through the periodic boundaries.

We follow the method developed by Livraghi et al.[55] to determine the percolation threshold from MD simulations and compare it to the prediction given by eq 14. Their estimate threshold is defined by the reduced molecular weight (RMW) and point of inflection of the largest-mass cluster. The RMW is defined as the molecular weight average of all clusters in the system except the largest one. The largest cluster's size is a more indirect measurement of gelation, where the moment at which the mass of the largest cluster starts to significantly outweigh the other clusters is used as the gelation point. Here, we use both methods to get the most reliable estimate of the critical sticker conversion (p) needed to achieve gelation. The use of both methods is justified considering that the values of p were varied in steps of 0.05, which may be too low of a resolution for an exact match between theory and simulations.

Figure 8 demonstrates the two methods described above for the estimation of the gel point at a vitrimer fraction $\phi = 0.5$. The result obtained from the maximum of the RMW curve predicts a lower critical value for the onset of percolation, $p = 0.4$. On the other hand, the inflection point of the largest cluster size estimates a higher onset ($p = 0.475$). Using these two methods of determining the sol–gel transition, we can provide a confidence interval for percolation in the simulated systems. This result can then be compared to the prediction given by the mean-field theory in eq 14.

4. RESULTS AND DISCUSSION

4.1. Comparison between Theory and Simulations

We are finally ready to compare the theoretical phase-diagram predictions with the results of simulations. We initialize the free energy with parameter values dictated by the simulations: choosing a discretization such that every bead fills exactly one lattice site, the parameters $M = N = 20$ and $s = 5$ are straightforward from Section 3. The free parameter k was estimated by visually fitting to the simulation results, and found to be

https://doi.org/10.1021/acs.macromol.6c00893
Macromolecules XXXX, XXX, XXX–XXX

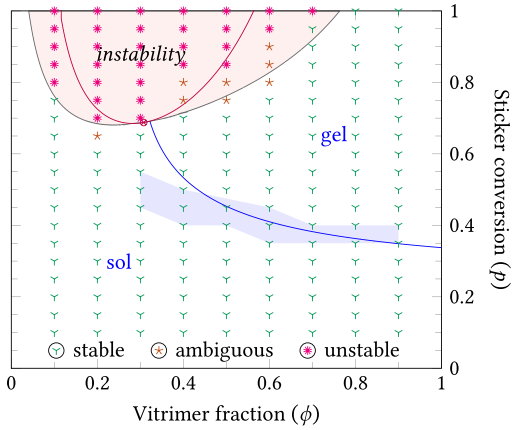

Figure 9. Phase diagram from theory (lines) and from simulations (symbols). Three classes of stability are shown: stable, clearly phase separated, and ambiguous or borderline. The free-energy parameters are $M = N = 20$, $s = 5$, and $k = 0.48$. This figure shows the same theoretical data as Figure 3, plotted on square axes to maximize visibility of the simulation points for small ϕ. The percolation transition seen in simulations (Section 3.4) appears as a pale blue band.

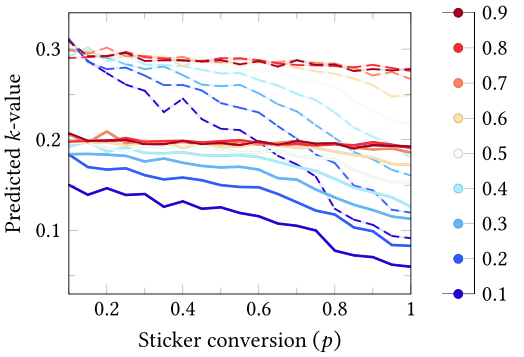

Figure 10. Value of the left-hand side of eq 6 as a function of p for all values of ϕ. Solid lines indicate calculations involving only nearest-neighbor cross-links, dashed lines correspond to calculations involving all same-chain cross-links.

somewhere around one half: $k = 0.48 \pm 0.08$. (This motivated the earlier choice of values in Figure 3.) For better visibility of the simulated data, we refrain from using 'pinched axes' in favor of a more traditional square plot, giving Figure 9.

Note that on square axes, tie-lines are *not* straight line segments, and thus are not shown. On the same plot, we show the spinodal curve (red line, inside the region of instability), the plait point (symbol ⊗) and the mean-field percolation transition (blue line).

The results of simulations are split into three classes — stable, clearly phase separated, and borderline — and shown on Figure 9 using symbols. The confidence interval for the percolation transition, obtained using the methods in Section 3.4, is indicated by a pale blue region. The region forms a band around the theoretical prediction for $\phi \geq 0.5$, when the mean-field theory is expected to be most accurate; the agreement is worse for smaller values of ϕ, when same-chain bonds become important and the mean-field assumptions weaken.

Looking at the distribution of simulation results, we see that all systems which displayed clear phase separation in the simulations lie within the theoretical region of instability. There is some uncertainty near the boundary, due to the gradual onset of separation in simulations as the p-value increases (as discussed in Section 3.3). Nonetheless, we find very good agreement between theory and simulations at an appropriately chosen value for the free parameter k.

4.2. Consistency of the Local-Bonding Parameter

How reasonable is this fitted value $k \approx 0.48$? We can check consistency by calculating it in different ways. One is to use the result for Gaussian chains, eq 11, applied to a lattice based on the MC/MD beads. Here, the bond length is around the minimum of the FENE potential ($b \approx 0.96\,\sigma$); every bead is a statistical segment, so the Kuhn volume is that of a bead ($v_K = \frac{\pi}{6}\,\sigma^3$); and every lattice site corresponds to one bead ($v_0 = v_K$). Using these values in eq 11 gives $k \approx 0.39$, in agreement with the fitted uncertainty 0.48 ± 0.08.

Whilst the accuracy of this agreement is to some extent coincidental — for example, if instead of using as unit volume the size of a bead ($v_0 = v_K$) we had used the inverse number density of monomers in the simulation box ($v_0 = 1/\rho \approx 1.18\,\sigma^3$), the estimate would have risen to $k \approx 0.88$ — it remains heartening to find a result of the correct order of magnitude. This can be compared with another way to verify consistency, namely measuring the values of p and q directly in the simulations and using them to solve for k in eq 6. Limiting this analysis to systems which unequivocally do *not* undergo phase separation, we obtain $k \approx 0.20$ from the fraction of cross-links which are between nearest-neighbor stickers on the same chain. Note however that this is expected to be an underestimate: in the simulated systems, same-chain bonds are not limited to being between nearest-neighbor stickers, and can span the whole chain; nearest-neighbor bonds are thus less likely than they might be in a nearest-neighbor-only system. To compensate for this, we can imagine a different definition of q in simulations: instead of using the fraction of bonds which are between *nearest-neighbor* stickers, we can measure the fraction of bonds which are between *any two stickers on the same chain*. Using this alternative definition for q in eq 6 gives $k \approx 0.30$ on average. (Figure 10 shows the detail of the calculation for both q variants, plotting the equivalent k value for each simulated sticker conversion p and vitrimer volume fraction ϕ.) For stable systems, the predicted values of k remain approximately constant, and the value starts to drop as soon as instability sets in, since the single-phase percolation condition ceases to apply. As with the previous method, we find a value of the correct order of magnitude, though the estimate is now further from the fitted value.

A third method of controlling consistency is to return to the definition $k := \mathbb{P}\left[l_{N/s}\right] \times 4N/(sx)$. Assuming beads in the simulation are to a good approximation hexagonally packed, each sticker has roughly $x = 12 - 2 = 10$ free sites adjacent to it. The natural discretization — one bead per lattice volume — makes N/s the number of bead diameters between successive stickers. The only missing quantity is then $\mathbb{P}\left[l_{N/s}\right]$, the probability that two nearest-neighbor stickers are within a bond length of each other. This quantity can be obtained from the simulations by observing a system sure not to separate — e.g., $\phi = 0.9$ and $p = 0.5$ — and counting, amongst all nearest-neighbor sticker pairs, which proportion are less than a distance $2 \times 0.96\,\sigma$ apart. (In fact, to avoid interference from the cross-

https://doi.org/10.1021/acs.macromol.6c00893
Macromolecules XXXX, XXX, XXX–XXX

linking algorithms, we look only at beads on *homopolymer* chains spaced four bond lengths apart.) We find a probability $\mathbb{P}[l_4] \approx 0.3$, yielding a value $k = 0.48$.

4.3. Phase Diagram for a Realistic Blend

Comparison with simulations suggests good reason to be confident in the applicability of the theoretical model. In this section, we provide a phase diagram for a more realistic choice of parameters, inspired by a polystyrene-based vitrimer chemistry.

4.3.1. Steric Cross-Linker and Stopper. Thus far, we have approximated cross-linker and stopper moieties as 'phantom' objects, occupying no volume. Depending on the size of these two moieties, however, the approximation may have limited applicability. To relax this assumption, we split the vitrimer network into three types of component: the chain backbone (B), the cross-linker (C) and the stopper (D). Each component — or, for simplicity, 'species' — is considered to occupy a volume N_i in discretization units: the index i runs over the four species in our system, the remaining species (A) being the homopolymer chains. This gives four volume fractions ϕ_i of which to keep track.

Repeating the argument in Section 2 for a four-species system gives an intensive free energy

$$f = -\mathfrak{H}\left(\frac{s\phi_B}{N_B} - \frac{q}{p}\frac{\phi_C}{N_C}\right) + \sum_i \frac{\mathfrak{H}(\phi_i)}{N_i} + \left[\mathfrak{H}(1-q/p) + \mathfrak{H}(q/p) + \frac{q}{p}\log\left(\frac{2N_B}{esk}\right)\right]\frac{\phi_C}{N_C} \tag{19}$$

with $q \approx kp/(k + 2\phi_B)$, where the four volume fractions ϕ_i are related by the stoichiometric condition $s\phi_B/N_B = 2\phi_C/N_C + \phi_D/N_D$ and the — obvious — new volume balance, $\sum_i \phi_i = 1$. The degree of conversion is also updated to $p = 2N_B\phi_C/(sN_C\phi_B)$. In the interest of brevity, the derivation of these results is relegated to the supplementary information (Section A.3).

The consistency of eq 19 with the expressions in Sections 2 and 3 can be seen by (i) relabelling $N_A = M$ and $N_B = N$, (ii) setting $\phi_C = (sN_C/2N_B)\,\psi$ and $\phi_D = (sN_D/N_B)\,(\phi - \psi)$ and (iii) taking the volume balance $\sum_i \phi_i = 1$ in the limit of small cross-linker and stopper size ($sN_C \sim sN_D \ll N_B$) to claim that $\phi_B = \phi = 1 - \phi_A$. It can be verified that the result of this procedure is the simplified system discussed up to now. This consistency implies that the simplified model, wherein the cross-linker and stopper are 'phantom' objects, correctly accounts for the mobility of real, physical cross-linkers. In the full calculation, the cross-linkers' translational entropy is reduced by attaching the cross-linkers to stickers; the simpler calculation instead includes a combinatorial entropy of cross-linking, but the resulting contribution to the free energy is the same. The collapse of the two free energies — eqs 5 and 19 — in the limit of small cross-linker and stopper thus supports the intuition that the size of the cross-linker and stopper moieties has no impact on phase separation at zeroth order. In other words, the phase diagram varies continuously as the cross-linker size goes to zero.

Figure 1b showed the chemical structure of a polystyrene vitrimer–homopolymer melt, categorized into our four species A, B, C and D (based on dioxaborolane functional groups). The cutting point between B and C/D is chosen to be the point where the chemical bonds break during a cross-link exchange interaction. For such a system, what values should be used for the parameters N_i, $i \in \{A, \cdots, D\}$? Recall that the on-lattice parameters N_i are defined as the number of lattice sites occupied by a single representative of a given species. As such, they are equal to the volume occupied by that representative divided by the unit lattice-site volume: $N_i = v_i/v_0$. Therefore, it suffices to estimate the volume of one representative from each species, since the free energy is invariant under rescaling of the elementary lattice volume v_0.

Given degrees of polymerization dp_A and dp_B and vitrimer functionality s, the volume occupied by each species can be approximated by its mass. Counting atoms in Figure 1b gives

$$N_A = \mathrm{dp}_A \quad N_B = \mathrm{dp}_B + \frac{47}{52}s \quad N_C = 5/4 \quad N_D = 1 \tag{20}$$

where the parameters N_i are generated by scaling every mass by the same factor of 104 Da.

4.3.2. Longer Chains. The degrees of polymerization used for simulations — twenty beads, five stickers — are constrained by the numerical capacity of the computers at our disposal. In real applications, we might expect chains to have monomer counts somewhere in the thousands, and function sites numbering hundreds. We thus take our new-found, fully steric expressions and apply them to a system with chains orders of magnitude longer.

As a plausible example, we consider both homopolymer and vitrimer to have degree of polymerization $\mathrm{dp}_i = 1500$ and assume $s = 200$ stickers per vitrimer chain (corresponding to a molecular weight of 175 kDa for the vitrimer and 156 kDa for the polymer). For the unknown parameter k, we recall the scaling law in eq 11 and arbitrarily set $k = (s/N_B)^{1/2} \approx 0.34$. This is consistent — recall eq 8 — with values for the packing length ($P \approx 4$ Å) and root-mean-square end-to-end distance ($R_s \approx 20$ Å) experimentally measured for polystyrene.[56,57]

Figure 11 shows the resulting phase diagram. (Due to lack of convergence of the numerical method in the immediate neighborhood of the plait point, the binodal in that region is interpolated between the plait point and the first tie-lines identified.) The most striking feature is the onset of instability, which now occurs at much lower values of p. In the next section (Section 4.4), we show that this is consistent with scaling arguments for the simplified model of Section 2 when $s \gg 1$, which further suggests that, at zeroth order, the thermodynamics do not depend on the size of the cross-linker moiety.

4.4. Asymptotics of Highly Functionalized Chains

In the interest of quantifying the features of Figure 11, we look for the position of the plait point and percolation transition asymptotically for large numbers of sticker sites per chain (i.e., as $s \to \infty$). Their placement relative to each other will allow us to determine the generic appearance of the phase diagram in this limit. As the full model with steric cross-linker and stopper is analytically intractable, we return to the simpler model of eq 5 for the asymptotic analysis.

Finding the asymptotic behavior of the plait point as $s \to \infty$ requires simultaneously solving eqs 12 and 13 to first order in $1/s$. In the supplementary information, Part E, we find this gives

$$\phi = \frac{1}{1+\sqrt{N/M}} - \frac{3\sqrt{N/M}}{2s} + \mathcal{O}(s^{-2}) \tag{21}$$

https://doi.org/10.1021/acs.macromol.6c00893
Macromolecules XXXX, XXX, XXX–XXX

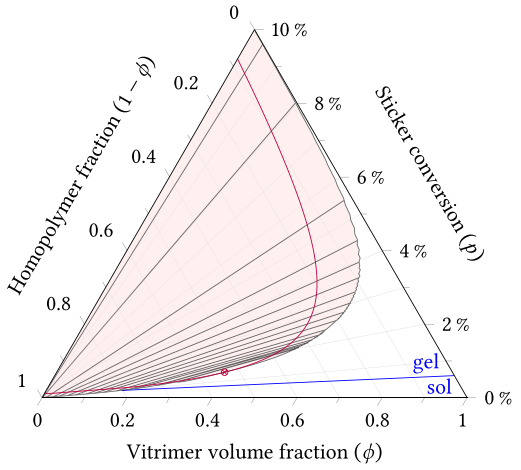

Figure 11. Phase diagram for a hypothetical polystyrene-based vitrimer melt with dioxaborolane-based cross-linker and stopper moieties, showing the gelation transition (blue), spinodal curve (red), binodal curve (gray), tie-lines (gray segments) and plait point (symbol ⊗). Parameter values are $\mathrm{dp_A} = \mathrm{dp_B} = 1500$, $s = 200$ and $k \approx 0.34$. Since the p-axis starts at zero, horizontal sections of this plot correspond to slices of constant ψ.

$$\psi = \frac{1}{2s}\left(2 + k + k\sqrt{N/M}\right) + \mathcal{O}\left(s^{-2}\right) \tag{22}$$

From eqs 21 and 22, we can compute the number of stickers per chain cross-linked to other chains at the plait point. This is the number of occupied sticker sites, ps, reduced by the number of sites cross-linked to the same chain, qs. To leading order in $1/s$, this gives

$$(p-q)s = 1 + \sqrt{\frac{N}{M}} + \mathcal{O}\left(\frac{1}{s}\right) \tag{23}$$

In other words, for chains of comparable length ($N \approx M$), a rule of thumb for the transition into immiscibility is that two stickers per chain be cross-linked to other chains. Comparing this to the rule of thumb for the percolation transition — which is one sticker per chain — we see that stability is only possible for networks which are loosely cross-linked, though it is possible to gel the system without phase separation as indicated in Figure 11.

When s becomes large, eq 14 for the percolation transition becomes $(p - q)s \approx 1$ to leading order, since $q \le p \in \mathcal{O}(1/s)$. Note the similarity to eq 23. Solving this explicitly gives

$$p \approx \frac{1}{s}\left(1 + \frac{k}{2\phi}\right) \tag{24}$$

at percolation. This is below the plait point but hits the region of instability fairly rapidly to the left of the plait point, since eq 24 diverges as $\phi \to 0$. Thus we see that, depending on the initial conditions, phase separation can either be into two gel phases or can span the percolation transition, giving both a sol and a gel phase. For large values of s, there is never separation into two sol phases.

The vast majority of the phase space, where p is large, separates into sol and gel. In particular, as $p \to 1$, tie-lines become arbitrarily close to being between $(\phi, \psi) = (0, 0)$ and $(1, 1)$, since the free energy in eq 5 becomes concave for $s \to \infty$ and $\psi \to \phi$. Therefore, highly cross-linked systems typically separate into (almost) pure polymer and vitrimer phases. In applications where the vitrimer is used as an additive to strengthen the polymer without losing recyclability, this means that adding more covalent bonds to the network will only cause it to separate more completely from the thermoplastic matrix.

4.5. Limitations of the Model

Certainly the primary limitation of the model presented is its pure-entropic nature. In a real system, configurations have enthalpy: due to the interaction between atomic potentials; due to compressibility of the sample; due to the effect of temperature; — none of this is accounted for in our model. Of these, the energetic interactions of adjacent atoms are a particularly important omission. In the simplest case of a melt of identical backbone chemistries, as the proportion of monomers which are functions ($s/\mathrm{dp_B}$) grows small, we expect the effect of energetic interactions to scale with the number of contacts between homopolymer and vitrimer backbone on one side, and cross-linker and stopper moieties on the other. Using the interaction parameter χ of Flory–Huggins solution theory, this scale is roughly $\chi s/N_B$. The energetic term will affect the position of the binodal line when it is comparable to the stable, Flory–Huggins term of the free energy, which scales as $\max\{N_A^{-1}, N_B^{-1}\}$. For equal chain lengths $N_A = N_B$, this suggests that the relevant parameter for energetic effects in our networks is χs, which is much less than the relevant parameter in homopolymeric melts χN_B. We thus expect energetic effects to be suppressed in vitrimeric melts.

Like others before it, this model assumes that functional sites are evenly distributed along the vitrimer chain. In practice, an ideal co-polymerization will lead to a random distribution of functional sites, and non-idealities such as variations in reactivity or co-monomer drift can lead to blockiness in site distribution or uneven distribution of sites between chains. This will inevitably affect the physics of the system.

Another limitation is the model's treatment of the weakly concentrated regime ($\phi \ll 1$). In the presence of an energetic interaction with the solvent/matrix, previous literature has suggested that the vitrimer chains would form globular structures.[12,13] We believe this mechanism to be absent in the entropic formalism presented in this paper. Nonetheless, a significant aspect of the entropic case has been neglected in our treatment: namely, the higher-order 'harmonics' of same-chain cross-linking, which drive chain collapse in real physical systems.[58] We neglected these under the assumption that they are suppressed by their polynomial entropic cost, their contribution to the partition function scaling as $(\text{loop length})^{-3/2}$. We know from eq 4 that the number of possible nearest-neighbor–only configurations on s sites with c cross-links is $(s - c)!/[c!\ (s - 2c)!]$, and from eq 2 that the total number of configurations on s sites with c cross-links is $s!/[2^c\ c!\ (s - 2c)!]$. This means that the proportion of configurations which are nearest-neighbor only is the ratio of the first to the second, or

$$\frac{2^c\ (s-c)!}{s!} \approx \exp\left[-c\log\left(\frac{s}{2}\right) + \mathcal{O}\left(\frac{c}{s}\right)\right] \tag{25}$$

This quantity vanishes factorially as s grows large, largely overtaking the suppression factor associated with non-nearest-neighbor cross-links. This leads us to suggest that as the number of functions

https://doi.org/10.1021/acs.macromol.6c00893
Macromolecules XXXX, XXX, XXX–XXX

on a given vitrimer chains grows, the cross-linking behavior of isolated vitrimer chains is not dominated by that between nearest-neighbor stickers, but exhibits cross-links between stickers of arbitrary separation along the backbone. This combinatorial effect will be compounded by the fact that a sort of 'economy of scale' is at play: once the vitrimer chain is already collapsed, longer-range cross-links are no longer so entropically expensive as they would originally have been. The topic of isolated vitrimer chains is still an open question for research to tackle.

Finally, we wish to highlight that the mean-field methods used in this article suffer the drawback that they are not spatially resolved: phases are treated as homogeneous throughout. This means that such a theory cannot be used to make meaningful statements about separation into micro-phases; yet if — e.g. — the cross-linker is strongly repelled by the vitrimer backbone, we expect the formation of spatially segregated clusters of cross-linked sites. An accurate treatment of such clusters may require the use of a fully-fledged field theory,[15] with the added complexity that such theories entail.

5. CONCLUSIONS

In this study, we have derived a mean-field model for the free energy of an associative covalent polymer network. From the free energy, quantitative predictions can be made for a wide range of melt compositions and cross-link fractions by using appropriate numerical methods.

The model's validity is supported by the agreement of molecular dynamics simulations with the phase diagram predicted by the theory. These simulations emulated the dynamics of vitrimer–polymer blends by combining a Kremer–Grest bead-spring model with a bespoke Monte-Carlo bond-exchange algorithm. Instability and percolation were detected by comparing features in the distribution and clustering of vitrimer beads within discrete subdomains of the simulation box; for instability, the variance in bead density and the spatial correlation of the subdomains' deviation from mean composition proved particularly useful in classifying edge cases. Since the vitrimer and homopolymer analogues were made chemically identical, any instability observed was solely a result of the entropic effect of cross-links between stickers.

We predict phase separation for a range of parameter values, even despite the exclusion of energetic effects. Stated differently: blends of otherwise non-interacting polymeric materials can become immiscible merely through the addition of a cross-linking mechanism. This prediction, though consistent with previous work on dissociative systems,[12,13] nonetheless has a novel aspect: only in *associative* systems is it possible to wholly disregard energetic mechanisms. The phenomena described herein are entirely entropic, and serve as a warning that affinity at a chemical level is in no way a guarantee that a polymer–vitrimer blend will remain homogeneously distributed.

Finally, we emphasize that phase separation sets in at low degrees of cross-linking — as few as two sites per chain when the vitrimer and polymer are equal in nature and length, not much more than the amount required for gelation — constituting an important physical limit to the use of vitrimers as a strength-enhancing additive.

■ ASSOCIATED CONTENT

Data Availability Statement

The source code and raw data for all the figures provided in this paper are freely available in the ReBond dataverse [URL https://dataverse.uclouvain.be/dataverse/rebond]. The Monte-Carlo bond-exchange logic is also available as an open-source PyPI package [URL https://pypi.org/project/MC-exchange/] installable through pip under the name MC-exchange. The first version of this manuscript was deposited on the preprint server arXiv [DOI https://doi.org/10.48550/arXiv.2603.25532]. For the purpose of open access, the authors have applied a Creative Commons Attribution (CC BY) license to any Author Accepted Manuscript version arising from this submission.

Supporting Information

The Supporting Information is available free of charge at https://pubs.acs.org/doi/10.1021/acs.macromol.6c00893.

Additional derivations and expressions for the free energy along with plots of the spatial correlation, density variance, and percolation transition data; citation numbers in the SI[59,60] refer to the bibliography of this paper (PDF)

■ AUTHOR INFORMATION

Corresponding Author

Alexandros A. Rispo Constantinou – *Department of Chemical, Materials and Production Engineering, University of Naples 'Federico II', Naples 80125, Italy; Bio- and Soft Matter, Institute of Condensed Matter and Nanosciences, Université catholique de Louvain, Louvain-La-Neuve 1348, Belgium;* orcid.org/0009-0007-2960-1589; Email: alexandrosandreas.constantinou@unina.it

Authors

Bálint Magyari – *Department of Chemical, Materials and Production Engineering, University of Naples 'Federico II', Naples 80125, Italy; Department of Materials Science and Engineering, University of Crete, Heraklion 70013, Greece;* orcid.org/0009-0007-2282-8043

Giovanni Iannirubertо – *Department of Chemical, Materials and Production Engineering, University of Naples 'Federico II', Naples 80125, Italy;* orcid.org/0000-0002-6963-8753

Evelyne van Ruymbeke – *Bio- and Soft Matter, Institute of Condensed Matter and Nanosciences, Université catholique de Louvain, Louvain-La-Neuve 1348, Belgium;* orcid.org/0000-0001-7633-0194

Daniel J. Read – *School of Mathematics, University of Leeds, Leeds LS2 9JT, U.K.;* orcid.org/0000-0003-1194-9273

Complete contact information is available at: https://pubs.acs.org/doi/10.1021/acs.macromol.6c00893

Notes

The authors declare no competing financial interest.

■ ACKNOWLEDGEMENTS

We thank Peiwen Ren and Lorenzo Contento for their advice on computing the lower convex envelope of a surface; Nathan van Zee for his cartoon of a vitrimer melt; and our colleagues from the ReBond network for fruitful discussions.

This work was funded by the European Union under the Horizon Europe grant [GA 101119786]. Simulations were carried out on the high-performance computing cluster 'IBiSCo' [PON 2014–2020, project code PIR01_00011].

A large language model (Google Gemini) was used by B. M. to assist in refining the Python scripts used for data analysis and to edit the manuscript for language and clarity. The authors rigorously reviewed and verified all LLM-generated outputs to ensure scientific accuracy and assume full responsibility for the final content.

■ REFERENCES

(1) Montarnal, D.; Capelot, M.; Tournilhac, F.; Leibler, L. Silica-like malleable materials from permanent organic networks. *Science* **2011**, *334*, 965–968.

(2) Zheng, J.; Png, Z. M.; Ng, S. H.; Tham, G. X.; Ye, E.; Goh, S. S.; Loh, X. J.; Li, Z. Vitrimers: current research trends and their emerging applications. *Mater. Today* **2021**, *51*, 586–625.

(3) Denissen, W.; Winne, J. M.; Du Prez, F. E. Vitrimers: permanent organic networks with glass-like fluidity. *Chem. Sci.* **2016**, *7*, 30–38.

(4) Wang, Z.; Gu, Y.; Ma, M.; Liu, Y.; Chen, M. Strengthening polyethylene thermoplastics through a dynamic covalent networking additive based on alkylboron chemistry. *Macromolecules* **2021**, *54*, 1760–1766.

(5) Torres, N.; Barzycki, D. C.; Bauer, Z. R.; Duclos, C.; Ricarte, R. G. Immiscible polydimethylsiloxane/polybutadiene vitrimer blends. *Macromolecules* **2026**.

(6) Winne, J. M.; Leibler, L.; Du Prez, F. E. Dynamic covalent chemistry in polymer networks: a mechanistic perspective. *Polym. Chem.* **2019**, *10*, 6091–6108.

(7) Han, H.; Xu, X. Poly(methyl methacrylate)–epoxy vitrimer composites. *J. Appl. Polym. Sci.* **2018**, *135*, 46307.

(8) Hayashi, M. Understanding vitrimer properties through various aspects of inhomogeneity. *Polym. J.* **2025**, *57*, 343–355.

(9) Ricarte, R. G.; Tournilhac, F.; Leibler, L. Phase separation and self-assembly in vitrimers: hierarchical mor phology of molten and semicrystalline polyethylene/dioxaborolane maleimide systems. *Macromolecules* **2019**, *52*, 432–443.

(10) De Heer Kloots, M. H. P.; Schoustra, S. K.; Dijksman, J. A.; Smulders, M. M. J. Phase separation in supramolec ular and covalent adaptable networks. *Soft Matter* **2023**, *19*, 2857–2877.

(11) Joosten, L. M. A.; Cassagnau, P.; Drockenmuller, E.; Montarnal, D. Synthesis, recycling and high-throughput reprocessing of phase-separated vitrimer-thermoplastic blends. *Adv. Funct. Mater.* **2024**, *34*, 2306882.

(12) Semenov, A. N.; Rubinstein, M. Thermoreversible gelation in solutions of associative polymers. 1. Statics. *Macromolecules* **1998**, *31*, 1373–1385.

(13) Dobrynin, A. V. Phase diagram of solutions of associative polymers. *Macromolecules* **2004**, *37*, 3881–3893.

(14) Smallenburg, F.; Leibler, L.; Sciortino, F. Patchy particle model for vitrimers. *Phys. Rev. Lett.* **2013**, *111*, 188002.

(15) Vigil, D. L.; Fredrickson, G. H.; Qin, J. Coherent state field theory for reversible gelation of star polymers. *Macromolecules* **2025**, *58*, 10920–10936.

(16) Fantoni, R.; Müller-Nedebock, K. K. Field-theoretical approach to a dense polymer with an ideal binary mixture of clustering centers. *Phys. Rev. E* **2011**, *84*, 011808.

(17) Tanaka, F. Comparative study on the models of thermoreversible gelation. *IJMS* **2022**, *23*, 10325.

(18) Chen, J.; Chen, E.; Yang, S. Gelation and phase separation in oppositely charged polyelectrolyte solutions: the formation of quadrupoles. *Macromolecules* **2025**, *58*, 11418–11428.

(19) Danielsen, S. P. O.; Semenov, A. N.; Rubinstein, M. Phase separation and gelation in solutions and blends of heteroassociative polymers. *Macromolecules* **2023**, *56*, 5661–5677.

(20) Prusty, D.; Pryamitsyn, V.; Olvera de la Cruz, M. Thermodynamics of associative polymer blends. *Macromolecules* **2018**, *51*, 5918–5932.

(21) Cappa, M.; Chiani, S.; Sciortino, F.; Rovigatti, L. A single-chain nanoparticle-based mean-field theory for associative polymers. *Macromolecules* **2026**, *59*, 6006–6015.

(22) Skorik, Yu. A.; Petrova, V. A.; Okatova, O. V.; Strelina, I. A.; Gasilova, E. R. Characterization of clusters and unimers in associating solutions of chitosan by dynamic and static light scattering. *Macromol. Chem. Phys.* **2016**, *217*, 1636–1644.

(23) Bawendi, M. G.; Freed, K. F.; Mohanty, U. A lattice model for self-avoiding polymers with controlled length distributions. II. Corrections to Flory–Huggins mean field. *J. Chem. Phys.* **1986**, *84*, 7036–7047.

(24) Foreman, K. W.; Freed, K. F. Influence of stiffness, monomer structure, and energetic asymmetries on polymer blend miscibilities: applications to polyolefins. *Macromolecules* **1997**, *30*, 7279–7295.

(25) Fredrickson, G. H.; Liu, A. J.; Bates, F. S. Entropic corrections to the Flory–Huggins theory of polymer blends: architectural and conformational effects. *Macromolecules* **1994**, *27*, 2503–2511.

(26) Kozuch, D.; Zhang, W.; Milner, S. Predicting the Flory–Huggins χ parameter for polymers with stiffness mismatch from molecular dynamics simulations. *Polymers* **2016**, *8*, 241.

(27) Zhang, W.; Gomez, E. D.; Milner, S. T. Predicting Flory–Huggins χ from simulations. *Phys. Rev. Lett.* **2017**, *119*, 017801.

(28) Zilman, A.; Kieffer, J.; Molino, F.; Porte, G.; Safran, S. A. Entropic phase separation in polymer-microemulsion networks. *Phys. Rev. Lett.* **2003**, *91*, 015901.

(29) Kremer, K.; Grest, G. S. Dynamics of entangled linear polymer melts: a molecular-dynamics simulation. *J. Chem. Phys.* **1990**, *92*, 5057–5086.

(30) Everaers, R.; Karimi-Varzaneh, H. A.; Fleck, F.; Hojdis, N.; Svaneborg, C. Kremer-Grest models for commodity polymer melts: linking theory, experiment, and simulation at the Kuhn scale. *Macromolecules* **2020**, *53*, 1901–1916.

(31) Behbahani, A. F.; Schmid, F. Relaxation dynamics of entangled linear polymer melts via molecular dynamics simulations. *Macromolecules* **2025**, *58*, 767–786.

(32) Cui, X.; Jiang, N.; Shao, J.; Zhang, H.; Yang, Y.; Tang, P. Linear and nonlinear viscoelasticities of dissociative and associative covalent adaptable networks: discrepancies and limits. *Macromolecules* **2023**, *56*, 772–784.

(33) Xia, J.; Kalow, J. A.; Olvera de la Cruz, M. Structure, dynamics, and rheology of vitrimers. *Macromolecules* **2023**, *56*, 8080–8093.

(34) Perego, A.; Lazarenko, D.; Cloitre, M.; Khabaz, F. Microscopic dynamics and viscoelasticity of vitrimers. *Macromolecules* **2022**, *55*, 7605–7613.

(35) Flory, P. J. *Principles of polymer chemistry, 9th printing 1975*; Cornell University Press: Ithaca, **1953**.

(36) Levin, O. *Discrete mathematics: an open introduction*, 3rd ed.; [Open Textbooks]: **2021**.

(37) Qin, J. Similarity of polymer packing in melts is dictated by N^{-}. *Macromolecules* **2024**, *57*, 1885–1892.

(38) Bobbili, S. V.; Milner, S. T. Measuring packing length in simulations for different polymer architectures. *J. Rheol.* **2021**, *65*, 1245–1253.

(39) Doi, M.; Edwards, S. F. *The theory of polymer dynamics*; International series of monographs on physics; Clarendon Press: Oxford, **1988**; p 391.

(40) Grosberg, Yu. A.; Khokhlov, A. R. *Statistical physics of macromolecules*; AIP series in polymers and complex materials; AIP Press: New York, **1994**; p 350.

(41) Shcherbakova, N.; Gerbaud, V.; Roger, K. Using the intrinsic geometry of binodal curves to simplify the computation of ternary liquid–liquid phase diagrams. *Entropy* **2023**, *25*, 1329.

(42) Tompa, H. *Polymer solutions*; Butterworths Scientific Publications: London, **1956**; p 325.

(43) Archer, A. J.; Goddard, B. D.; Sibley, D. N.; Rawlings, J. T.; Broadhurst, R.; Ouali, F. F.; Fairhurst, D. J. Experimental and theoretical bulk phase diagram and interfacial tension of ouzo. *Soft Matter* **2024**, *20*, 5889–5903.

(44) Qian, D.; Michaels, T. C. T.; Knowles, T. P. J. Analytical solution to the Flory–Huggins model. *J. Phys. Chem. Lett.* **2022**, *13*, 7853–7860.
(45) Qian, D.; Ausserwoger, H.; Sneideris, T.; Farag, M.; Pappu, R. V.; Knowles, T. P. J. Dominance analysis to assess solute contributions to multicomponent phase equilibria. *Proc. Natl. Acad. Sci. U. S. A.* **2024**, *121*, e2407453121.
(46) Ren, P. Convex hull construction of phase diagrams: a visual introduction. *Peiwen Ren*. https://pwren.me/blog/2023/phase-diagram/ (accessed Jan 24, 2025).
(47) Santra, A.; Dünweg, B.; Ravi Prakash, J. Universal scaling and characterization of gelation in associative polymer solutions. *J. Rheol.* **2021**, *65*, 549–581.
(48) Rubinstein, M.; Colby, R. H., *Polymer physics*; Oxford University Press: Oxford, **2003**; p 440.
(49) Weeks, J. D.; Chandler, D.; Andersen, H. C. Role of repulsive forces in determining the equilibrium structure of simple liquids. *J. Chem. Phys.* **1971**, *54*, 5237–5247.
(50) Thompson, A. P.; Aktulga, H. M.; Berger, R.; Bolintineanu, D. S.; Brown, W. M.; Crozier, P. S.; In 't Veld, P. J.; Kohlmeyer, A.; Moore, S. G.; Nguyen, T. D.; Shan, R.; Stevens, M. J.; Tranchida, J.; Trott, C.; Plimpton, S. J. LAMMPS — a flexible simulation tool for particle-based materials modeling at the atomic, meso, and continuum scales. *Comp. Phys. Comm.* **2022**, *271*, 108171.
(51) Perego, A.; Khabaz, F. Volumetric and rheological properties of vitrimers: a hybrid molecular dynamics and Monte Carlo simulation study. *Macromolecules* **2020**, *53*, 8406–8416.
(52) Perego, A.; Khabaz, F. Effect of bond exchange rate on dynamics and mechanics of vitrimers. *J. Polym. Sci.* **2021**, *59*, 2590–2602.
(53) Metropolis, N.; Rosenbluth, A. W.; Rosenbluth, M. N.; Teller, A. H.; Teller, E. Equation of state calculations by fast computing machines. *J. Chem. Phys.* **1953**, *21*, 1087–1092.
(54) Manousiouthakis, V. I.; Deem, M. W. Strict detailed balance is unnecessary in Monte Carlo simulation. *J. Chem. Phys.* **1999**, *110*, 2753–2756.
(55) Livraghi, M.; Höllring, K.; Wick, C. R.; Smith, D. M.; Smith, A.-S. An exact algorithm to detect the percolation transition in molecular dynamics simulations of cross-linking polymer networks. *J. Chem. Theory Comput.* **2021**, *17*, 6449–6457.
(56) Fetters, L. J.; Lohse, D. J.; Graessley, W. W. Chain dimensions and entanglement spacings in dense macro molecular systems. *J. Polym. Sci. B Polym. Phys.* **1999**, *37*, 1023–1033.
(57) Unidad, H. J.; Goad, M. A.; Bras, A. R.; Zamponi, M.; Faust, R.; Allgaier, J.; Pyckhout-Hintzen, W.; Wischnewski, A.; Richter, D.; Fetters, L. J. Consequences of increasing packing length on the dynamics of polymer melts. *Macromolecules* **2015**, *48*, 6638–6645.
(58) Berda, E. B.; Foster, E. J.; Meijer, E. W. Toward controlling folding in synthetic polymers: fabricating and characterizing supramolecular single-chain nanoparticles. *Macromolecules* **2010**, *43*, 1430–1437.
(59) Röttger, M.; Domenech, T.; van der Weegen, R.; Breuillac, A.; Nicolaý, R.; Leibler, L. High-performance vitrimers from commodity thermoplastics through dioxaborolane metathesis. *Science* **2017**, *356*, 62–65.
(60) Ge, S.; Evans, C. M. Influence of segmental dynamics on bond exchange in imine vitrimers with different polymer backbones and cross-linkers. *Macromolecules* **2025**, *58*, 4043–4058.

https://doi.org/10.1021/acs.macromol.6c00893
Macromolecules XXXX, XXX, XXX–XXX